Improved Dielectric Response of Solids: Combining the Bethe-Salpeter Equation with the Random Phase Approximation

Amalie H. Søndersted[*], Mikael Kuisma, Jakob K. Svaneborg, Mark Kamper Svendsen, and Kristian S. Thygesen

CAMD, Computational Atomic-scale Materials Design, Department of Physics,
Technical University of Denmark, 2800 Kgs. Lyngby, Denmark

The Bethe-Salpeter equation (BSE) can provide an accurate description of low-energy optical spectra of insulating crystals—even when excitonic effects are important. However, due to high computational costs it is only possible to include a few bands in the BSE Hamiltonian. As a consequence, the dielectric screening given by the real part of the dielectric function can be significantly underestimated by the BSE. Here, we show that universally accurate optical response functions can be obtained by combining a four-point BSE-like equation for the irreducible polarizability with a two-point Dyson equation that includes the higher-lying transitions within the random phase approximation. The new method is referred to as BSE+. It has a computational cost comparable to the BSE but a much faster convergence with respect to the size of the electron-hole basis. We use the method to calculate refractive indices and electron energy loss spectra for a test set of semiconductors and insulators. In all cases the BSE+ yields excellent agreement with experimental data across a wide frequency range and outperforms both the BSE and the random phase approximation.

The current state of the art for calculating optical absorption spectra of solids from first principles is based on many-body perturbation theory [1–7]. In a first step, the quasiparticle (QP) band structure is calculated within the GW approximation. In a second step, the two-particle (four-point) Bethe-Salpeter Equation (BSE) is solved within a limited space of electron-hole (e–h) transitions. The dimension of the BSE Hamiltonian is $N_c N_v N_k$, where $N_{c/v}$ is the number of conduction (valence) bands used to form the e-h basis and N_k is the number of k points. The scaling of this matrix means that in practice it is only possible to include a few bands close to the Fermi energy. This is sufficient for describing the low-energy excitations and the imaginary part of the dielectric function in the corresponding frequency range, but the lack of higher-lying excitations means that the real part is underestimated even at low frequencies.

The high computational cost of the BSE approach, which persists even with the best-scaling implementations [8–13], has motivated attempts to construct exchange-correlation (xc) kernels (f_{xc}) that can account for excitonic effects within the time-dependent density functional theory (TDDFT) [14] formalism [15–26]. The advantage of this approach is that the f_{xc} is a two-point function, which renders the Dyson equation much simpler, and allows one to include transitions up to very high energies.

The simplest approximation sets $f_{xc} = 0$, which is the random phase approximation (RPA). The RPA can yield a reasonably accurate description of the optical response of bulk metals and semiconductors, but it fails to account for excitons, which are important in systems with weak screening such as insulators and low-dimensional materials [27,28].

Attempts to go beyond the RPA with two-point xc kernels include the parameter free bootstrap kernel [15], which is based on a postulated (approximate) relation between f_{xc} and the macroscopic dielectric constant ε_M. The nanoquanta kernel [16] yields absorption spectra in very good agreement with BSE but at almost the same computational cost. The long-range correction kernel [17] of the simple form $f_{xc} = -\alpha/q^2$ is computationally efficient but depends on the parameter α.

Thus, the current situation is that one can either solve the four-point BSE to obtain an accurate description of the low-energy excitations but an underestimated screening (due to the neglect of high-energy transitions), or one can use the two-point TDDFT formalism to obtain a better description of screening at the cost of a more approximate description of excitonic effects.

In this Letter, we show how the BSE and RPA methods can be combined in a seamless manner to yield a practical scheme for calculating the optical response function of a solid that includes high-energy transitions and at the same time accounts for electron-hole correlations in the low-energy excitations. The new method is referred to as BSE+ and has a computational cost comparable to the BSE. Based on a small test set of semiconductors and insulators, the BSE+ is shown to yield refractive indices and electron

energy loss functions in significantly better agreement with experiments than both BSE and RPA.

We first recall the basic equations of the BSE. The excitation energies and associated two-particle wave functions are obtained by solving the eigenvalue equation [29]

$$\sum_{S'} \mathcal{H}(\mathbf{q})_{SS'} A_{S'}^\lambda(\mathbf{q}) = E^\lambda(\mathbf{q}) A_S^\lambda(\mathbf{q}), \tag{1}$$

where $\mathbf{q}$ is the momentum transfer and $S = \{n, m, \mathbf{k}\}$ and $S' = \{n', m', \mathbf{k}'\}$ are indices of the e-h basis. The Hamiltonian matrix takes the form

$$\mathcal{H}_{SS'}(\mathbf{q}) = (\varepsilon_{m\mathbf{k}+\mathbf{q}} - \varepsilon_{n\mathbf{k}})\delta_{SS'} - (f_{m\mathbf{k}+\mathbf{q}} - f_{n\mathbf{k}})K_{SS'}(\mathbf{q}). \tag{2}$$

Here, $f_{n\mathbf{k}}$ is the occupation function and $\varepsilon_{n\mathbf{k}}$ is the Kohn-Sham eigenvalue of band n with momentum $\mathbf{k}$. For singlet excitations, the kernel is

$$K_{SS'}(\mathbf{q}) = 2V_{SS'}^{\mathrm{SR}}(\mathbf{q}) - W_{SS'}(\mathbf{q}), \tag{3}$$

where $V_{SS'}^{\mathrm{SR}}$ is the short-range Coulomb interaction (obtained by setting the $\mathbf{G} = \mathbf{G}' = 0$ component in a plane-wave basis to zero) and $W_{SS'}$ is the static screened e-h interaction [7]. The retarded polarizability can be expanded in terms of the solutions to Eq. (1),

$$\tilde{P}_{SS'}(\mathbf{q}, \omega) = 2\sum_\lambda A_S^\lambda(\mathbf{q}) A_{S'}^\lambda(\mathbf{q})^* \times \left(\frac{f_{m\mathbf{k}+\mathbf{q}} - f_{n\mathbf{k}}}{\omega - E_\lambda + i\eta} - \frac{f_{m'\mathbf{k}'+\mathbf{q}} - f_{n'\mathbf{k}'}}{\omega + E_\lambda + i\eta} \right), \tag{4}$$

where η is a small positive number and we have employed the Tamm-Dancoff approximation [30] (TDA) under which the eigenvectors $A^\lambda(\mathbf{q})$ are orthogonal (note that the λ sum runs only over the positive excitation energies). Contracting the four-point polarizability to a two-point function and Fourier transforming yields

$$\tilde{P}_{\mathbf{G}\mathbf{G}'}(\mathbf{q}, \omega) = \frac{1}{\Omega} \sum_{SS'} \rho_S(\mathbf{G}) \tilde{P}_{SS'}(\mathbf{q}, \omega) \rho_{S'}(\mathbf{G}')^*, \tag{5}$$

where $\mathbf{G}$ is a reciprocal lattice vector, Ω is the crystal volume, and

$$\rho_S(\mathbf{G}) = \rho_{n\mathbf{k}}^{m\mathbf{k}+\mathbf{q}}(\mathbf{G}) = \langle \psi_{n\mathbf{k}} | e^{-i(\mathbf{q}+\mathbf{G})\mathbf{r}} | \psi_{m\mathbf{k}+\mathbf{q}} \rangle, \tag{6}$$

where $|\psi_{n\mathbf{k}}\rangle$ are the Kohn-Sham eigenstates. In the optical limit, it can be shown that

$$\lim_{\mathbf{q}\to 0} \rho_{n\mathbf{k}}^{m\mathbf{k}+\mathbf{q}}(\mathbf{0}) = \frac{i\mathbf{q} \cdot \langle \psi_{n\mathbf{k}} | \nabla | \psi_{m\mathbf{k}} \rangle}{\varepsilon_{n\mathbf{k}} - \varepsilon_{m\mathbf{k}}}. \tag{7}$$

We have introduced a tilde in Eq. (4) to indicate that the sum in practice only runs over a limited set of e-h transitions corresponding to the bands (and k points) used to construct $\mathcal{H}_{SS'}$. We shall denote this set of transitions by $\mathcal{T}$.

In practice, it is only possible to converge the imaginary part of $\tilde{P}$ up to a few electron volts above the band gap. It then follows from the Kramers-Kronig relations that the real part cannot be converged even at low frequencies. To address these issues, we introduce a BSE+ polarizability, capturing excitonic effects at the BSE level within the $\mathcal{T}$ transition manifold while accounting for high-energy transitions at the RPA level, thereby ensuring better convergence of both real and imaginary parts across all frequencies.

We start by defining an irreducible polarizability $\tilde{P}^{\mathrm{irr}}$ satisfying the following Dyson equation:

$$\tilde{P}_{SS'}^{\mathrm{irr}}(\mathbf{q}, \omega) = \tilde{P}_{SS'}^0(\mathbf{q}, \omega) - \frac{1}{2} \sum_{S_1 S_2} \tilde{P}_{SS_1}^0(\mathbf{q}, \omega) W_{S_1 S_2}(\mathbf{q}) \tilde{P}_{S_2 S'}^{\mathrm{irr}}(\mathbf{q}, \omega). \tag{8}$$

In practice, this response function is obtained from Eq. (4) by solving the eigenvalue equation (1) with $V^{\mathrm{SR}} = 0$ in Eq. (3). In the above equation, $\tilde{P}^0$ is the noninteracting (Kohn-Sham) polarizability in the e-h basis and with the sum over bands limited to the transitions $\mathcal{T}$. The contracted and Fourier transformed P^0 takes the form

$$P_{\mathbf{G}\mathbf{G}'}^0(\mathbf{q}, \omega) = \frac{2}{\Omega} \sum_{\mathbf{k},n,m} (f_{n\mathbf{k}} - f_{m\mathbf{k}+\mathbf{q}}) \times \frac{\rho_{n\mathbf{k}}^{m\mathbf{k}+\mathbf{q}}(\mathbf{G}) \rho_{n\mathbf{k}}^{m\mathbf{k}+\mathbf{q}}(\mathbf{G}')^*}{\omega + \varepsilon_{n\mathbf{k}} - \varepsilon_{m\mathbf{k}+\mathbf{q}} + i\eta}. \tag{9}$$

Next, we replace $\tilde{P}^0$ by P^0 (with no constraint on the sum over bands) to obtain

$$P_{\mathbf{G}\mathbf{G}'}^{\mathrm{irr}}(\mathbf{q}, \omega) = \tilde{P}_{\mathbf{G}\mathbf{G}'}^{\mathrm{irr}}(\mathbf{q}, \omega) - \tilde{P}_{\mathbf{G}\mathbf{G}'}^0(\mathbf{q}, \omega) + P_{\mathbf{G}\mathbf{G}'}^0(\mathbf{q}, \omega). \tag{10}$$

Finally, we obtain the BSE+ result for the polarizability by solving the Dyson equation

$$P_{\mathbf{G}\mathbf{G}'}^{\mathrm{BSE+}}(\mathbf{q}, \omega) = P_{\mathbf{G}\mathbf{G}'}^{\mathrm{irr}}(\mathbf{q}, \omega) + \sum_{\mathbf{G}_1 \mathbf{G}_2} P_{\mathbf{G}\mathbf{G}_1}^{\mathrm{irr}}(\mathbf{q}, \omega) V_{\mathbf{G}_1 \mathbf{G}_2}^{\mathrm{SR}}(\mathbf{q}) P_{\mathbf{G}_2 \mathbf{G}'}^{\mathrm{BSE+}}(\mathbf{q}, \omega). \tag{11}$$

We note that the BSE polarizability follows from Eq. (11) by replacing P^{irr} by $\tilde{P}^{\mathrm{irr}}$. Moreover, by replacing V^{SR} by the full Coulomb interaction V, we obtain the full density-density response function within the BSE+ approximation. Finally, we stress that within the BSE+ the TDA is only
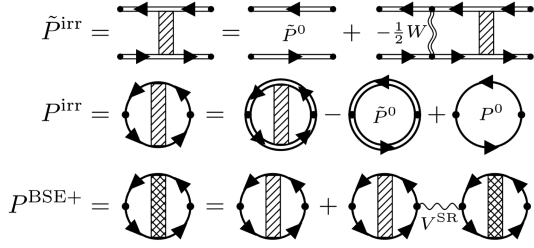
FIG. 1. Feynman diagrams representing Eqs. (8),(10), (11). Double fermion lines represent propagators restricted to the transition space $\mathcal{T}$, whereas single fermion lines represent full propagators. The double wiggly line represents the screened interaction W and the single wiggly line is the short-range part of the bare Coulomb interaction V^{SR}.

applied for the BSE part (calculation of the irreducible polarizability) while the RPA treatment of the high-energy transitions includes the coupling between resonant and antiresonant transitions, i.e., it does not invoke the TDA. Equations (8), (10), (11), which constitute the BSE+ method, can be illustrated by the Feynman diagrams in Fig. 1.

Previous work has stressed the importance of screening the e-h exchange in the BSE by transitions outside the $\mathcal{T}$ subspace [31,32]. Our work goes beyond the previous work by including such transitions explicitly in the response function.

To evaluate the performance of the BSE+ method, we use it to calculate the refractive index of a set of solids and compare it to experimental data and results of the BSE and RPA methods. We have calculated the refractive indices of silicon (Si), molybdenum disulfide (MoS_2), hexagonal boron nitride (hBN), and titanium dioxide (TiO_2) in both the rutile and anatase phases. The structures were set up using experimental lattice parameters from [33] (Si), [34] (rutile TiO_2), [35] (anatase TiO_2), [36] (MoS_2), and [37] (hBN). For rutile TiO_2 the refractive index has been calculated for two orientations, namely in plane and out of plane, corresponding to the electric field being orthogonal and parallel to the c axis, respectively. For MoS_2, hBN, and anatase TiO_2 we have only considered the in-plane refractive index. The refractive index depends on both the real and imaginary part of the dielectric function, and it therefore offers a way of evaluating the accuracy of both of these simultaneously. The refractive index is determined from the relation

$$n(\omega) = \text{Re}\left(\sqrt{\varepsilon_M(\omega)}\right), \tag{12}$$

where $\varepsilon_M(\omega)$ is the macroscopic dielectric function

$$\varepsilon_M(\omega) = 1 - \lim_{\mathbf{q}\to 0}\frac{4\pi}{q^2}P_{\mathbf{G}=\mathbf{G}'=0}(\mathbf{q},\omega). \tag{13}$$

The divergence of the Coulomb potential is cancelled in the optical limit by exploiting Eq. (7).

To further evaluate the ability of the BSE+ to describe high frequency responses and plasmonic excitations, we calculate the electron energy loss spectrum (EELS) defined as

$$\text{EELS}(\omega) = -\text{Im}(1/\varepsilon_M(\omega)). \tag{14}$$

We have implemented functions to determine $\tilde{P}^{irr}$, $\tilde{P}^0$, and P^0 in the BSE and RPA codes in GPAW [38,39]. For each material, we performed a DFT calculation [40] using the PBE exchange-correlation functional [41] to determine the ground state wave functions and eigenvalues. All the computational details can be found in the Supplemental Material [42].

For the BSE and BSE+ calculations, we explicitly account for the screened e-h interaction within the transition space $\mathcal{T}$. We include a given band n in $\mathcal{T}$, if and only if $\varepsilon_n(\mathbf{k})$ lies within ΔE_B of the valence band maximum or the conduction band minimum for at least one k point. This ensures that *at least* all transitions up to the energy $E_{gap}^{QP} + \Delta E_B$ are included in $\mathcal{T}$. For all materials we have used $\Delta E_B = 2$ eV, except for TiO_2 anatase where we have used $\Delta E_B = 1.6$ eV due to the larger number of atoms in the unit cell (12 atoms). The corresponding number of bands is listed for each material in the Supplemental Material [42].

As a final comment, PBE is known to underestimate band gaps. As our primary focus has not been on obtaining accurate QP gaps, we have handled this issue by utilizing a scissors operator to adjust the band gaps, aligning the lowest peak observed in the refractive index calculated with

TABLE I. Fitted direct QP band gaps and low-energy refractive indices from experiments and calculations using BSE+, BSE, and RPA. The experimental data are not available down to the static limit, so we have specified the energy, ω_{min}, at which the refractive index of each material has been read off. In the last row we show the mean absolute percentage error (MAPE) of the calculations compared to experiments.

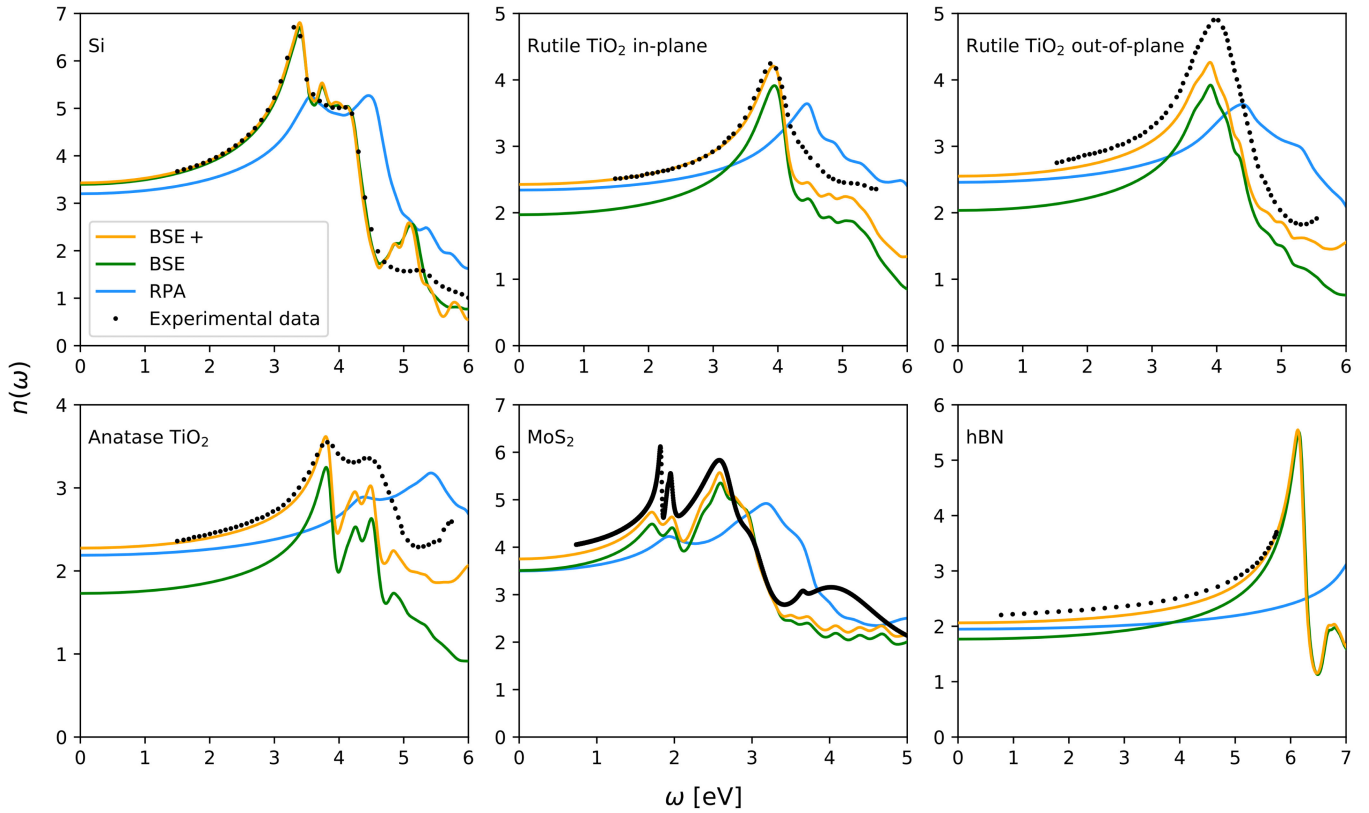| Material | E_{dir}^{QP} [eV] | ω_{min} [eV] | $n(\omega_{min})$ | | | |
			Exp.	BSE+	BSE	RPA
Si	3.35	1.50	3.67	3.66	3.63	3.36
Rutile TiO_2 in plane	3.30	1.49	2.51	2.51	2.06	2.40
Rutile TiO_2 out of plane	3.30	1.53	2.75	2.64	2.13	2.52
Anatase TiO_2	4.05	1.50	2.36	2.34	1.80	2.23
hBN	7.06	0.78	2.20	2.07	1.78	1.95
MoS_2	1.87	0.73	4.05	3.86	3.61	3.56
MAPE from exp. [%]				2.62	15.87	8.36

FIG. 2. Refractive indices calculated with BSE+ (orange), BSE (green), and RPA (blue). The experimental refractive indices are marked with black dots, and are obtained from [47] (Si), [48] (TiO$_2$), [49] (hBN), and [50] (MoS$_2$). For MoS$_2$, n was calculated from the experimental dielectric function.

BSE with the lowest peak in the refractive index observed in the experimental data. The fitted direct QP band gaps, E_{dir}^{QP}, can be found in Table I. The same value for the direct QP band gap, or equivalently the scissors shift, is used for RPA, BSE, and BSE+. In the Supplemental Material [42] we show that there is good agreement between the fitted direct QP band gaps and direct GW band gaps found in the literature [44–46].

The refractive indices of all five crystals calculated with BSE+, BSE, and RPA together with experimental data are shown in Fig. 2. The values of the refractive indices at the lowest energies available in the experimental data, ω_{min}, can be found in Table I.

With the exception of Si, which is well-described by both BSE and BSE+, the BSE underestimates the refractive index across all frequencies. This is due to the neglect of transitions beyond the limited set $\mathcal{T}$. The RPA misses the excitonic peaks and underestimates the refractive index for frequencies below the band gap. This is due to the neglect of attractive e-h interactions. In all cases, the BSE+ captures the exciton peaks and provides an accurate description of the refractive index over the entire frequency range surpassing both the BSE and RPA in performance with no additional computational cost compared to BSE. We note that the BSE+ presents only little or no
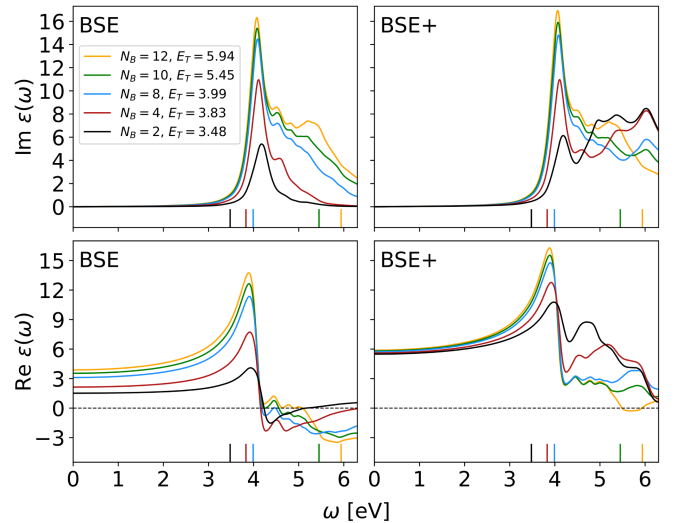

FIG. 3. Convergence of the in-plane real and imaginary parts of the dielectric function of rutile TiO$_2$ with respect to the number of bands included in the BSE and BSE+ calculations. N_B is the total number of bands in the BSE/BSE+ calculations divided equally between valence and conduction bands. The parameter E_T denotes the energy below which all e-h transitions are included given the number of bands in the calculation, and the values are marked with vertical lines.
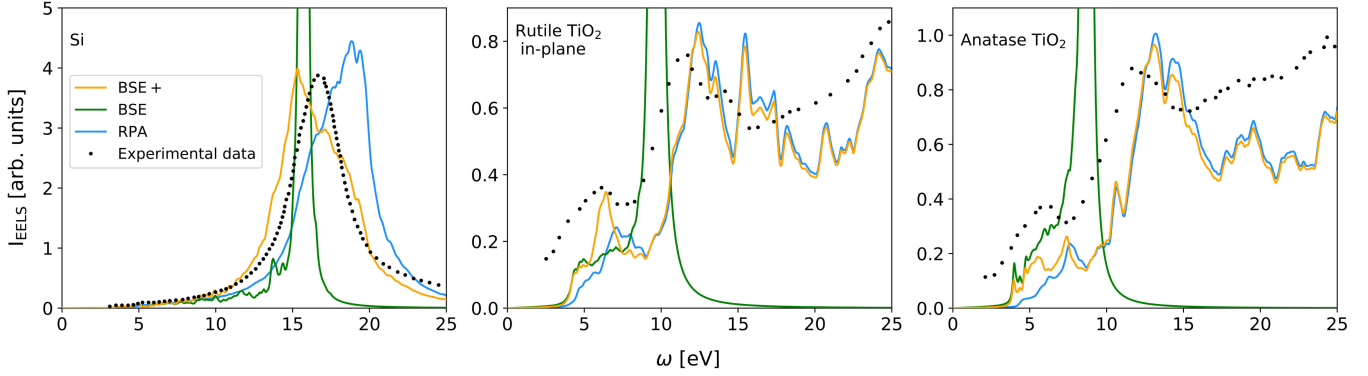
FIG. 4. EEL spectra calculated with BSE+ (orange), BSE (green), and RPA (blue). The experimental data are marked with black dots and are obtained from [51] (Si), and [52] (TiO$_2$).

improvement over the BSE in terms of predicting the shape and location of the low-energy excitonic peaks. Instead, it provides a better description of the peak height. We further note that the in-plane BSE and BSE+ calculations of rutile TiO$_2$ are more accurate than the out-of-plane calculations. The specific reasons for this discrepancy remain unknown. A key parameter in the theory is the number of bands included in the transition space $\mathcal{T}$. As the number of bands included in $\mathcal{T}$ increases, the BSE and BSE+ results will eventually become identical, as illustrated in the plot of Si in Fig. 2, although the convergence is very slow and not feasible to achieve in practice for all but the simplest materials. Figure 3 shows the in-plane dielectric function of rutile TiO$_2$ obtained with BSE and BSE+ as a function of the size of $\mathcal{T}$. The latter is represented by the parameter E_T, denoting the highest energy below which all e-h transitions are included in $\mathcal{T}$.

From Fig. 3 we see that the low-energy real part of the dielectric function from BSE converges very slowly with the number of bands, while BSE+ yields a converged value already with two bands. The imaginary part of the dielectric function is more localized and thus both the BSE and BSE+ seem converged up to E_T. The faster convergence of the BSE+ calculations with the number of bands stems from the following: while BSE completely neglects all transitions beyond $\mathcal{T}$, the BSE+ merely neglects the e-h attraction (W) in the transitions beyond $\mathcal{T}$, which is obviously a much more gentle approximation. It can be seen that the dielectric function from BSE+ generally is well converged up to the transition energy threshold E_T, which provides a simple means to estimate and control the energy range in which a BSE+ calculation can be expected to be converged.

We now turn to the description of EELS. In Fig. 4 we show the $q = 0$ EELS of Si and TiO$_2$ in the rutile and anatase phases as calculated with RPA, BSE, BSE+, and compared to experimental data. In all cases, the BSE falls short due to the lack of high-energy excitations. As also seen for the refractive indices, the RPA-based EELS do not capture the excitonic features in the low-energy range. On the other hand, the BSE+ reproduces both the gross features in the experimental spectra, which are mainly governed by plasmonic excitations, and the finer structures of excitonic origin around the band edge. In the case of Si, the e-h attraction does not produce distinct excitonic peaks, but redshifts the large plasmon peak (as compared to the RPA result). This shift is captured by the BSE+ despite the plasmon energy ($\sim$17 eV) being much larger than the threshold energy of 2 eV used to select the bands to be included in $\tilde{P}^{\mathrm{irr}}$. For anatase and rutile TiO$_2$ the BSE+ result is close to the RPA (and experiments) for energies above 10 eV, while the excitonic peaks around 4–7 eV are better described by BSE+.

In conclusion, we have introduced the BSE+ method, which extends the well-known BSE method by including transitions outside the active BSE e-h space. The additional transitions are included at the RPA level, which makes it possible to complete the transition space without increasing the computational cost. We have shown that relative to standard BSE and RPA, the BSE+ method significantly improves the description of dielectric screening, refractive indices, and EEL spectra because it accounts for excitons and plasmons simultaneously. The method can be further extended by using any two-point TDDFT kernel to account for xc effects among the additional transitions. The method could also form the basis for total energy calculations based on the adiabatic connection fluctuation dissipation theorem, where a response function with an accurate description of low-energy excitations and inclusion of high-energy transitions is of key importance [53].

*Contact author: amhso@dtu.dk

[1] G. Onida, L. Reining, and A. Rubio, Electronic excitations: Density-functional versus many-body green's-function approaches, Rev. Mod. Phys. **74**, 601 (2002).

[2] G. Onida, L. Reining, R. W. Godby, R. Del Sole, and W. Andreoni, *Ab initio* calculations of the quasiparticle and absorption spectra of clusters: The sodium tetramer, Phys. Rev. Lett. **75**, 818 (1995).

[3] S. Albrecht, L. Reining, R. Del Sole, and G. Onida, *Ab initio* calculation of excitonic effects in the optical spectra of semiconductors, Phys. Rev. Lett. **80**, 4510 (1998).

[4] L. X. Benedict, E. L. Shirley, and R. B. Bohn, Theory of optical absorption in diamond, Si, Ge, and GaAs, Phys. Rev. B **57**, R9385 (1998).

[5] M. Rohlfing and S. G. Louie, Electron-hole excitations in semiconductors and insulators, Phys. Rev. Lett. **81**, 2312 (1998).

[6] A. Marini, C. Hogan, M. Grüning, and D. Varsano, Yambo: An *ab initio* tool for excited state calculations, Comput. Phys. Commun. **180**, 1392 (2009).

[7] J. Yan, K. W. Jacobsen, and K. S. Thygesen, Optical properties of bulk semiconductors and graphene/boron nitride: The bethe-salpeter equation with derivative discontinuity-corrected density functional energies, Phys. Rev. B **86**, 045208 (2012).

[8] M. Grüning, A. Marini, and X. Gonze, Implementation and testing of Lanczos-based algorithms for random-phase approximation eigenproblems, Comput. Mater. Sci. **50**, 2148 (2011).

[9] F. Fuchs, C. Rödl, A. Schleife, and F. Bechstedt, Efficient O(N2) approach to solve the Bethe-Salpeter equation for excitonic bound states, Phys. Rev. B **78**, 085103 (2008).

[10] D. Kammerlander, S. Botti, M. A. L. Marques, A. Marini, and C. Attaccalite, Speeding up the solution of the Bethe-Salpeter equation by a double-grid method and Wannier interpolation, Phys. Rev. B **86**, 125203 (2012).

[11] Y. Gillet, M. Giantomassi, and X. Gonze, Efficient on-the-fly interpolation technique for Bethe–Salpeter calculations of optical spectra, Comput. Phys. Commun. **203**, 83 (2016).

[12] D. Rocca, Y. Ping, R. Gebauer, and G. Galli, Solution of the Bethe-Salpeter equation without empty electronic states: Application to the absorption spectra of bulk systems, Phys. Rev. B **85**, 045116 (2012).

[13] I. M. Alliati, D. Sangalli, and M. Grüning, Double k-grid method for solving the Bethe-Salpeter equation via Lanczos approaches, Front. Chem. **9**, 763946 (2022).

[14] E. Runge and E. K. U. Gross, Density-functional theory for time-dependent systems, Phys. Rev. Lett. **52**, 997 (1984).

[15] S. Sharma, J. K. Dewhurst, A. Sanna, and E. K. U. Gross, Bootstrap approximation for the exchange-correlation kernel of time-dependent density-functional theory, Phys. Rev. Lett. **107**, 186401 (2011).

[16] F. Sottile, V. Olevano, and L. Reining, Parameter-free calculation of response functions in time-dependent density-functional theory, Phys. Rev. Lett. **91**, 056402 (2003).

[17] L. Reining, V. Olevano, A. Rubio, and G. Onida, Excitonic effects in solids described by time-dependent density-functional theory, Phys. Rev. Lett. **88**, 066404 (2002).

[18] V. U. Nazarov and G. Vignale, Optics of semiconductors from meta-generalized-gradient-approximation-based time-dependent density-functional theory, Phys. Rev. Lett. **107**, 216402 (2011).

[19] S. Rigamonti, S. Botti, V. Veniard, C. Draxl, L. Reining, and F. Sottile, Estimating excitonic effects in the absorption spectra of solids: Problems and insight from a guided iteration scheme, Phys. Rev. Lett. **114**, 146402 (2015).

[20] P. E. Trevisanutto, A. Terentjevs, L. A. Constantin, V. Olevano, and F. Della Sala, Optical spectra of solids obtained by time-dependent density functional theory with the jellium-with-gap-model exchange-correlation kernel, Phys. Rev. B **87**, 205143 (2013).

[21] Z.-h. Yang, F. Sottile, and C. A. Ullrich, Simple screened exact-exchange approach for excitonic properties in solids, Phys. Rev. B **92**, 035202 (2015).

[22] Y.-M. Byun and C. A. Ullrich, Assessment of long-range-corrected exchange-correlation kernels for solids: Accurate exciton binding energies via an empirically scaled bootstrap kernel, Phys. Rev. B **95**, 205136 (2017).

[23] A. V. Terentjev, L. A. Constantin, and J. M. Pitarke, Gradient-dependent exchange-correlation kernel for materials optical properties, Phys. Rev. B **98**, 085123 (2018).

[24] S. Cavo, J. A. Berger, and P. Romaniello, Accurate optical spectra of solids from pure time-dependent density functional theory, Phys. Rev. B **101**, 115109 (2020).

[25] D. R. Gulevich, Y. V. Zhumagulov, V. K. Kozin, and I. V. Tokatly, Excitonic effects in time-dependent density functional theory from zeros of the density response, Phys. Rev. B **107**, 165118 (2023).

[26] J. A. Berger, Fully parameter-free calculation of optical spectra for insulators, semiconductors, and metals from a simple polarization functional, Phys. Rev. Lett. **115**, 137402 (2015).

[27] C. D. Spataru, S. Ismail-Beigi, L. X. Benedict, and S. G. Louie, Excitonic effects and optical spectra of single-walled carbon nanotubes, Phys. Rev. Lett. **92**, 077402 (2004).

[28] F. Hüser, T. Olsen, and K. S. Thygesen, How dielectric screening in two-dimensional crystals affects the convergence of excited-state calculations: Monolayer MoS_2, Phys. Rev. B **88**, 245309 (2013).

[29] M. Gatti and F. Sottile, Exciton dispersion from first principles, Phys. Rev. B **88**, 155113 (2013).

[30] R. M. Martin, L. Reining, and D. M. Ceperley, *Interacting Electrons* (Cambridge University Press, Cambridge, England, 2016).

[31] T. Deilmann and K. S. Thygesen, Important role of screening the electron-hole exchange interaction for the optical properties of molecules near metal surfaces, Phys. Rev. B **99**, 045133 (2019).

[32] L. X. Benedict, Screening in the exchange term of the electron-hole interaction of the Bethe-Salpeter equation, Phys. Rev. B **66**, 193105 (2002).

[33] J. Harl, L. Schimka, and G. Kresse, Assessing the quality of the random phase approximation for lattice constants and atomization energies of solids, Phys. Rev. B **81**, 115126 (2010).

[34] U. Diebold, The surface science of titanium dioxide, Surf. Sci. Rep. **48**, 53 (2003).

[35] J. K. Burdett, T. Hughbanks, G. J. Miller, J. W. Richardson, and J. V. Smith, Structural-electronic relationships in

inorganic solids: Powder neutron diffraction studies of the rutile and anatase polymorphs of titanium dioxide at 15 and 295 K, J. Am. Chem. Soc. **109,** 3639 (1987).

[36] B. Schonfeld, J. J. Huang, and S. C. Moss, Anisotropic mean-square displacements (MSD) in single crystals of 2h- and 3r-MoS_2, Acta Crystallogr. **39,** 404 (1983).

[37] W. Paszkowicz, J. Pelka, M. Knapp, T. Szyszko, and S. Podsiadlo, Lattice parameters and anisotropic thermal expansion of hexagonal boron nitride in the 10–297.5 K temperature range, Appl. Phys. A **75,** 431 (2002).

[38] J. Enkovaara, C. Rostgaard, J. J. Mortensen *et al.*, Electronic structure calculations with GPAW: A real-space implementation of the projector augmented-wave method, J. Phys. Condens. Matter **22,** 253202 (2010).

[39] J. J. Mortensen, A. H. Larsen, M. Kuisma *et al.*, GPAW: An open Python package for electronic structure calculations, J. Chem. Phys. **160,** 092503 (2024).

[40] W. Kohn and L. J. Sham, Self-consistent equations including exchange and correlation effects, Phys. Rev. **140,** 1138 (1965).

[41] J. P. Perdew, K. Burke, and M. Ernzerhof, Generalized gradient approximation made simple, Phys. Rev. Lett. **77,** 3865 (1996).

[42] See Supplemental Material, which includes Ref. [43], at http://link.aps.org/supplemental/10.1103/PhysRevLett.133.026403 for an overview of computational details, and a comparison of the quasi-particle band gaps used in this work with GW band gaps from the literature.

[43] H. J. Monkhorst and J. D. Pack, Special points for brillouin-zone integrations, Phys. Rev. B **12,** 5188 (1976).

[44] I.-H. Chu, J. P. Trinastic, Y.-P. Wang, A. G. Eguiluz, A. Kozhevnikov, T. C. Schulthess, and H.-P. Cheng, All-electron self-consistent GW in the matsubara-time domain: Implementation and benchmarks of semiconductors and insulators, Phys. Rev. B **93,** 125210 (2016).

[45] W. Kang and M. S. Hybertsen, Quasiparticle and optical properties of rutile and anatase TiO_2, Phys. Rev. B **82,** 085203 (2010).

[46] T. Cheiwchanchamnangij and W. R. L. Lambrecht, Quasiparticle band structure calculation of monolayer, bilayer, and bulk MoS_2, Phys. Rev. B **85,** 205302 (2012).

[47] D. E. Aspnes and A. A. Studna, Dielectric functions and optical parameters of Si, Ge, Gap, GaAs, GaSb, InP, InAs, and InSb from 1.5 to 6.0 eV, Phys. Rev. B **27,** 985 (1983).

[48] J. Jellison, G. E, L. A. Boatner, and J. D. Budai, Spectroscopic ellipsometry of thin film and bulk anatase (TiO_2), J. Appl. Phys. **93,** 9537 (2003).

[49] A. Segura, L. Artús, R. Cuscó, T. Taniguchi, G. Cassabois, and B. Gil, Natural optical anisotropy of h-BN: Highest giant birefringence in a bulk crystal through the mid-infrared to ultraviolet range, Phys. Rev. Mater. **2,** 024001 (2018).

[50] B. Munkhbat, P. Wróbel, T. J. Antosiewicz, and T. O. Shegai, Optical constants of several multilayer transition metal dichalcogenides measured by spectroscopic ellipsometry in the 300–1700 nm range: High index, anisotropy, and hyperbolicity, ACS Photonics **9,** 2398 (2022).

[51] J. Stiebling, Optische eigenschaften des einkristallinen siliziums aus elektronenenergieverlustmessungen, Z. Phys. B **31,** 355 (1978).

[52] M. Launay, F. Boucher, and P. Moreau, Evidence of a rutile-phase characteristic peak in low-energy loss spectra, Phys. Rev. B **69,** 035101 (2004).

[53] T. Olsen and K. S. Thygesen, Static correlation beyond the random phase approximation: Dissociating H2 with the Bethe-Salpeter equation and time-dependent GW, J. Chem. Phys. **140** (2014).